第 43 卷 第 4 期 焊 接 学 报 Vol. 43(4):86 − 93
2022 年 4 月 TRANSACTIONS OF THE CHINA WELDING INSTITUTION April 2022

焊丝成分对 5E61 铝合金 TIG 焊接头组织和性能的影响

毛晓东[1]， 谷宁杰[1]， 宋小雨[1]， 任思蒙[1]， 路丽英[2]， 李虎田[1]
(1. 中铝材料应用研究院有限公司, 北京, 102209; 2. 东北轻合金有限公司, 哈尔滨, 150060)

摘要: 为研究焊丝成分对 5E61 铝合金船板焊接接头组织和性能影响, 试验采用 Wire-1561, Wire-5B71 和 Wire-5E613 种焊丝对 4 mm 厚 5E61-H116 铝合金船板进行非熔化极惰性气体保护焊 (tungsten inert gas welding, TIG 焊), 并分析了焊接接头的表面形貌、成形质量、微观组织和力学性能. 结果表明, 在相同的焊接工艺下, 3 种焊丝接头焊缝成形质量良好, 焊缝中心无肉眼可见气孔. 不同焊丝接头焊缝区显微组织差异明显, Wire-5B71 焊缝晶粒最小, Wire-5E61 焊缝晶粒次之, Wire-1561 焊缝晶粒最大. 由于 Mg 元素的固溶强化和 Er 元素的细晶强化, Wire-5E61 接头焊缝区显微硬度最大. 对接头试样进行拉伸测试, 接头断裂位置主要沿熔合线附近的柱状晶区, 此位置显微硬度最低. Wire-1561, Wire-5B71 和 Wire-5E61 3 种焊丝接头抗拉强度分别为 322, 323 和 338 MPa, 焊接系数分别为 0.83, 0.84 和 0.88, 断后伸长率分别为 13.0%, 14.5% 和 14.5%, 满足实际工程应用.

创新点: (1) 提出通过匹配焊丝成分来提高船用高镁铝合金的焊接强度.
(2) 揭示了焊丝中 Mg, Er, Sc 元素对 5E61 铝合金 TIG 焊接头组织的影响规律.

关键词: 5E61 铝合金; TIG 焊; 微观组织; 力学性能
中图分类号: TG 457.1 **文献标识码:** A **doi:** 10.12073/j.hjxb.20211024001

0 序言

随着船舶、海洋工程的大型化、轻量化发展, 船舶用铝合金朝着轻质、高强方向发展. 由于船舶材料服役环境复杂, 对铝合金的强度、耐蚀性提出了更高要求. 5E61 铝合金是在常规 1561 铝合金基础上加入 Er 元素, 使其具有更高的强度和更好的耐蚀性能, 是新一代船舶用高强高耐蚀铝合金[1-2]. 船舶用铝离不开配套的连接技术, 目前针对 5E61 铝合金连接方面的研究主要集中在熔化焊, 焊接方法主要采用最常见的非熔化极惰性气体保护焊 (tungsten inert-gas welding, TIG 焊) 与熔化极惰性气体保护焊 (melt inert-gas welding, MIG 焊)[3-6]. 王虎等人[7]对新型 Al-Mg-Mn-Er 合金薄板进行 TIG 填丝焊接, 研究焊接热输入对接头组织性能的影响, 焊接系数最高可达 71.4%. 闫德俊等人[8]采用双面双弧 TIG 焊方法对 1561 铝合金进行了焊接, 发现焊缝区域存在特殊的组织不均匀性. 闫朝阳等人[9]采用穿孔等离子立焊方法对厚度为 4 mm 的 5E61 铝合金板材进行了焊接试验, 焊接接头焊缝处硬度达到母材硬度的 85% 以上.

以上针对 5E61 铝合金的焊接主要集中在焊接工艺研究, 对不同焊丝成分对焊缝组织及接头力学性能的影响未开展系统研究, 国内外未见相关报道. 因此, 文中采用 TIG 焊方法, 选用合金牌号为 1561, 5B71, 5E61 3 种成分焊丝 (以下标记为 Wire-1561, Wire-5B71, Wire-5E61), 对 4 mm 厚 5E61 铝合金船板进行焊接, 研究不同焊丝成分对焊缝组织和接头力学性能的影响, 为船舶实际焊接作业及焊材选择提供理论依据.

1 试验方法

试验所用基材为轧制 5E61 铝合金船板, 规格为 300 mm × 150 mm × 4 mm. 选用 Wire-1561, Wire-5B71, Wire-5E61 3 种合金牌号焊丝, 焊丝直径均为 1.2 mm. 5E61 基材及 3 种焊丝化学成分如表 1 所示.

收稿日期: 2021 − 10 − 24
基金项目: 国家重点研发计划项目 (2021YFB3704200)

表 1　5E61 基材及 3 种焊丝化学成分 (质量分数，%)

Table 1　Chemical compositions of 5E61 base material and three kinds of welding wire

材料	Si	Fe	Cu	Mn	Mg	Zn	Zr	Er	Sc	Al
5E61基材	0.15	0.12	0.01	0.91	5.91	0.01	0.12	0.19	—	余量
Wire-1561	0.05	0.08	0.02	0.94	5.69	0.01	0.08	—	—	余量
Wire-5B71	0.03	0.11	0.01	0.01	6.02	0.02	0.12	—	0.34	余量
Wire-5E61	0.03	0.15	0.01	0.88	6.23	0.04	0.11	0.35	—	余量

采用 Fronius Magic Wave TIG 焊机进行焊接，接头形式为对接焊，板材间隙为 1.2 mm，无需开坡口，单面焊双面成形. 试验前，用钢丝刷对基材进行打磨去除氧化膜，并用丙酮擦拭待焊区域，去除灰尘和油污等，以保证焊接质量. 焊接过程中采用工业纯氩 (纯度不小于 99%) 作为保护气体保护焊接熔池，并根据大量试验获得较优的焊接工艺参数，如表 2 所示.

表 2　焊接工艺参数

Table 2　Welding parameter

氩气流量 Q/(L·min^{-1})	焊接电流 I/A	焊接速度 v/(m·min^{-1})	板材间隙 d/mm
12	170～180	0.18	1.2

采用 Leica CH-9435 型体式显微镜对焊缝表面及纵截面进行拍照，并利用 image pro plus 图形测试软件对焊缝几何尺寸进行测量统计. 采用 AG-X Plus-10kN 型万能试验机测试不同焊丝成分的 TIG 焊接头力学性能，拉伸试样垂直于焊缝方向，且焊缝的轴线位于试样平行段的中间，拉伸速度为 1 mm/min，每组测试 5 个平行试样并取平均值. 采用 Fisher HM 2000 型显微硬度仪测量显微硬度，加载载荷为 0.98 N，保载时间为 15 s，由焊缝中心向两侧每隔 1 mm 取点测试.

对基材及焊接接头试样进行阳极覆膜，采用 Axio Scope A1 型光学显微镜进行微观组织观察. 采用配有能谱仪 (energy dispersive spectrometer, EDS) 和电子背散射衍射 (electron backscattered diffraction, EBSD) 探头的 TESCAN MIR3 型场发射扫描电镜对拉伸断口形貌、第二相成分以及焊缝处晶粒组织进行分析. EBSD 样品经打磨、机械抛光后，采用 $HClO_4$ + CH_3OH (体积比为 1∶9) 的腐蚀液进行电解抛光. 采用 Empyream 型 X 射线衍射仪 (X-ray diffractomer, XRD) 对 5E61 基材及焊接接头焊缝区进行物相分析.

2　试验结果与分析

2.1　焊缝成形

图 1 为 3 组焊丝接头焊缝正、反面表面形貌. 从图 1 可以看出，在相同的焊接工艺下，3 种焊丝形成的焊缝质量稳定，正面形成均匀细小的鱼鳞纹，反面熔深充分，形成水滴熔池，实现单面焊双面成形. 图 2 为焊缝纵截面形貌及几何尺寸. 从图 2a 可以看出，焊缝成形优良，呈轴对称分布；中心处无明显的气孔缺陷，零星的微小气孔只存在焊缝表面. 将 3 组焊缝上熔宽、下熔宽、上余高和下余高进行测量统计，结果如图 2b 所示. 3 种焊丝焊接接头几何尺寸接近，波动较小，说明焊接工艺稳定，焊缝成形质量好.

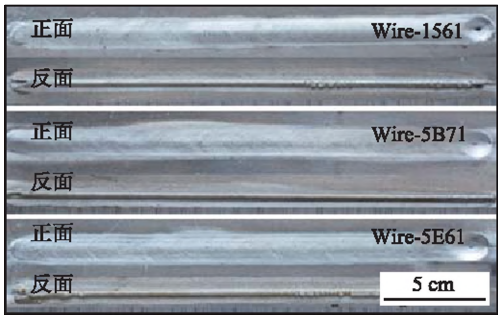

图 1　焊接接头表面形貌

Fig. 1　Surface morphology of welded joints

2.2　焊接接头显微组织

图 3 为 5E61 基材晶粒取向分布图及晶界统计分布图. 对原始 5E61 基材沿轧制方向进行 EBSD 观察，结果如图 3a 所示. 原始基材经冷轧后进行不完全退火，变形组织发生部分再结晶形成等轴组织；部分纤维组织发生合并长大变宽的情况，纤维组织出现分节，形成长径比约为 4 的再结晶晶粒；边界处的小晶粒数量增多. 由图 3b 可知，组织中仍存在大量的低角度晶界 (2°～15°代表低角度晶界，

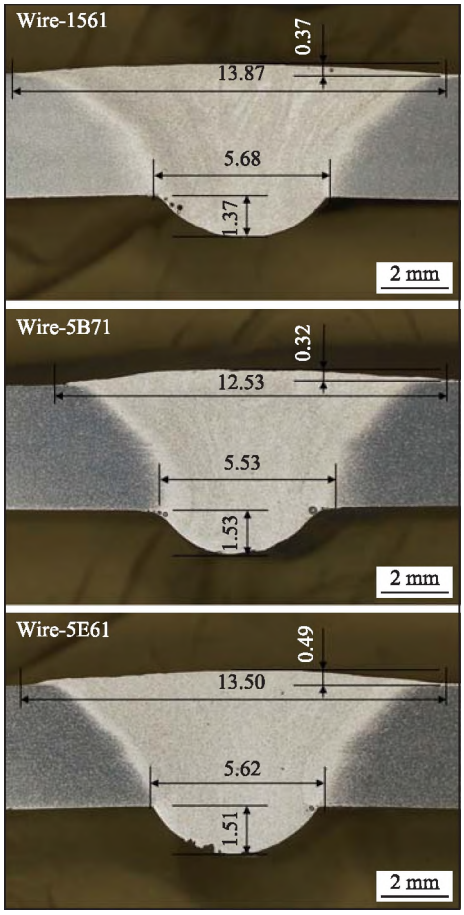

(a) 纵截面

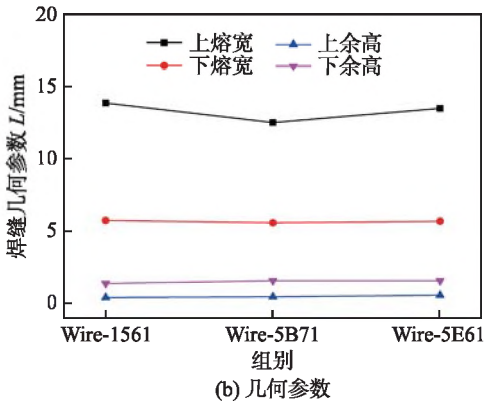

(b) 几何参数

图 2 焊缝纵截面及几何参数

Fig. 2 Longitudinal section and geometry parameter of welding lines. (a) longitudinal section; (b) geometry parameter

low angle grain boundaries, LAGBs; 高于 15°代表高角度晶界, high angle grain boundaries, HAGBs), 占比 59.8%, 经过不完全退火后, 板材组织保留部分轧制位错形成的亚晶界, 该组织既能充分释放轧制过程材料的内应力, 又保证了基材的力学性能.

图 4 为不同焊丝焊接接头的金相覆膜组织. 可以看出, 焊接接头分为焊缝区 (welding zone, WZ)、熔合区 (fusion zone, FZ) 以及热影响区 (heat affected

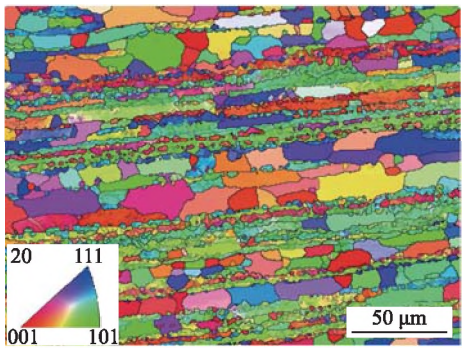

(a) 晶粒取向分布

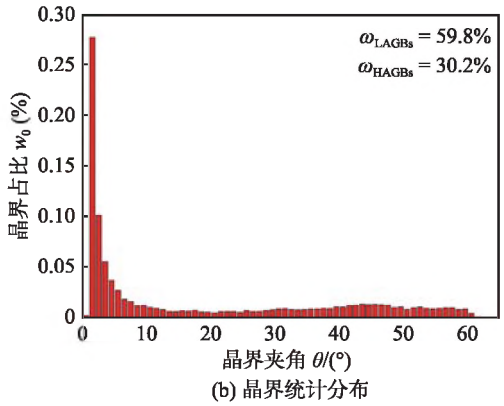

(b) 晶界统计分布

图 3 5E61 基材晶粒取向分布及晶界统计分布

Fig. 3 Grain orientation distribution map and grain boundary angle distributions map of 5E61 base material. (a) grain orientation distribution; (b) grain boundary angle distribution

zone, HAZ)3 部分. 焊缝区呈现典型的铸造组织特征, 中心位置呈等轴晶形貌. 在焊缝区与热影响区之间存在一定宽度的过渡区即熔合区, 该区域晶粒具有明显的晶粒取向, 从焊缝区指向热影响区, 形成长条状组织, 且尺寸不均匀. 3 组接头熔合区宽度接近, 从图中测出约为 180 ~ 200 μm.

图 5 为 3 种焊丝形成的焊接接头焊缝区及热影响区 EBSD 晶粒取向分布. 将各组接头的焊缝区及热影响区低角度晶界占比进行统计, 结果如图 6 所示. 从图 6 可以看出, 3 组接头热影响区低角度晶界占比 (ω_{LAGBs}) 较基材明显下降, 均在 35% ~ 38% 范围内. 这是由于 TIG 焊高的热输入使得原基材未完全再结晶组织发生了二次退火, 再结晶程度进一步提高, 冷变形过程产生的位错等亚结构湮灭, 晶界主要以高角度再结晶晶界形式存在. 从图 5 可以看出, 不同焊丝接头焊缝区晶粒大小差异明显. 通过 HKL Channel 5 软件计算, Wire-1561 接头晶粒最大, 约为 45 μm; Wire-5E61 接头次之, 约为 26 μm; Wire-5B71 接头晶粒尺寸最小, 约为 9 μm. 对比 3 组接头焊缝区 ω_{LAGBs} 可以发现, Wire-5E61 接头

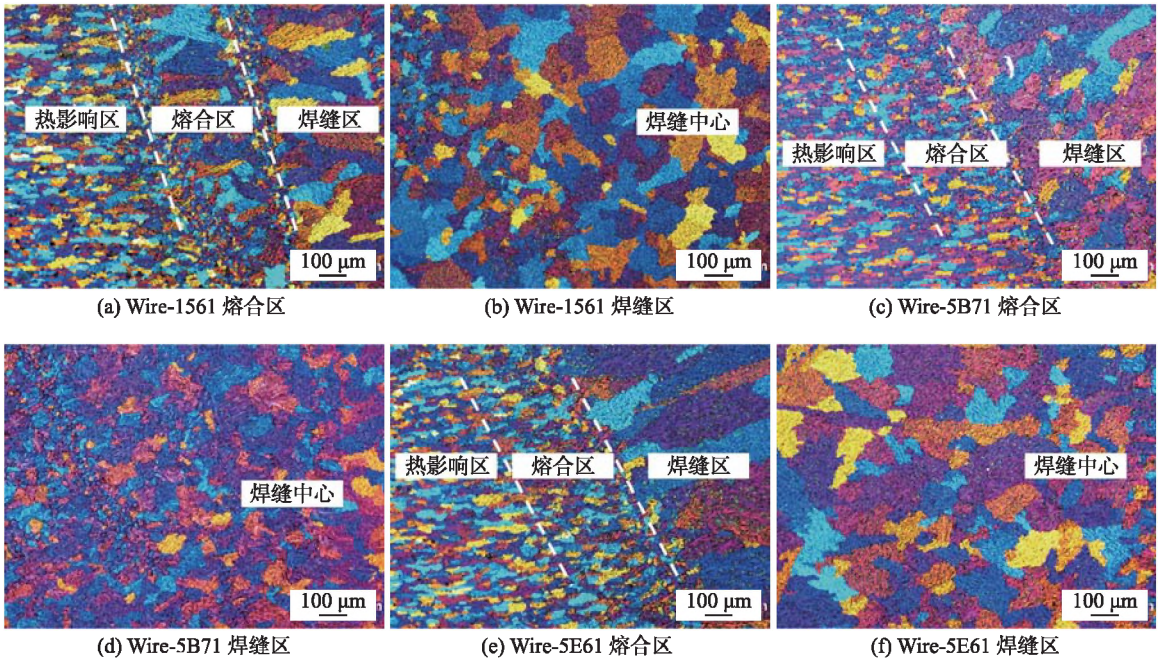

(a) Wire-1561 熔合区　(b) Wire-1561 焊缝区　(c) Wire-5B71 熔合区

(d) Wire-5B71 焊缝区　(e) Wire-5E61 熔合区　(f) Wire-5E61 焊缝区

图 4　焊接接头的金相组织

Fig. 4　Microstructure of welded joints. (a) FZ of Wire-1561; (b) WZ of Wire-1561; (c) FZ of Wire-5B71; (d) WZ of Wire-5B71; (e) FZ of Wire-5E61; (f) WZ of Wire-5E61

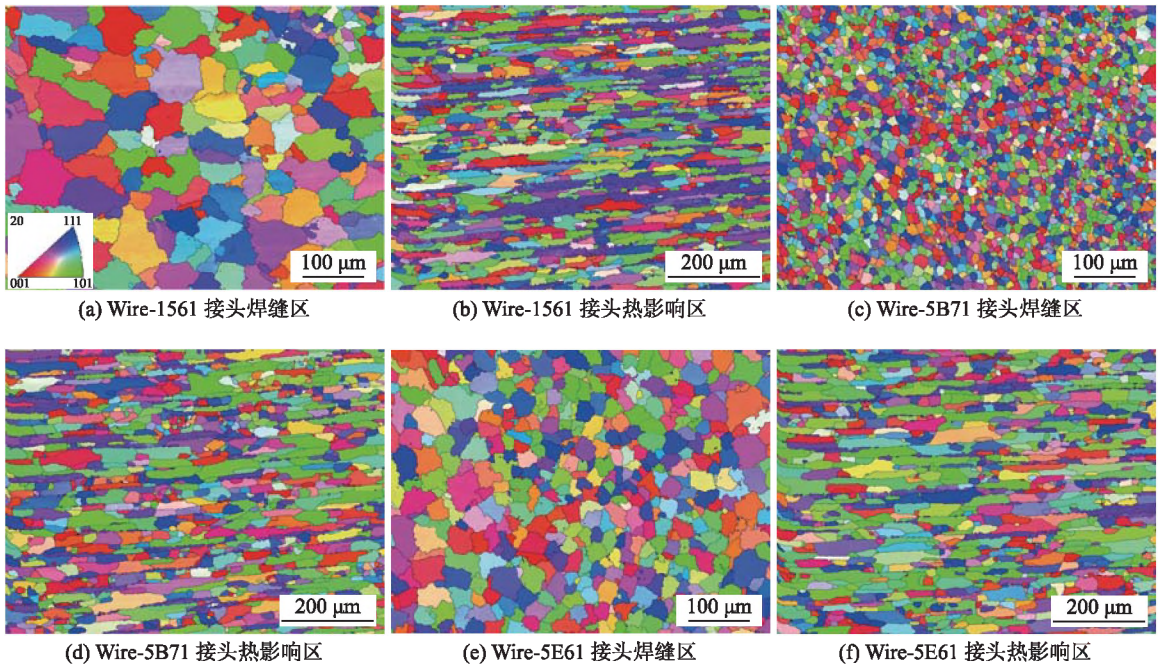

(a) Wire-1561 接头焊缝区　(b) Wire-1561 接头热影响区　(c) Wire-5B71 接头焊缝区

(d) Wire-5B71 接头热影响区　(e) Wire-5E61 接头焊缝区　(f) Wire-5E61 接头热影响区

图 5　不同焊丝接头焊缝及热影响区的晶粒取向分布图

Fig. 5　Orientation distribution maps of WZ and HAZ of welded joints with different welding wires. (a) WZ of Wire-1561; (b) HAZ of Wire-1561; (c) WZ of Wire-5B71; (d) HAZ of Wire-5B71; (e) WZ of Wire-5E61; (f) HAZ of Wire-5E61

ω_{LAGBs} 最小，Wire-5B71 接头次之，Wire-1561 接头最大. 这是由于 Wire-5E61 中 Mg 元素含量最高，β(Mg_2Al_3) 相数量较多，且焊丝中含有 Er 元素，焊后在焊缝区形成含 Er 弥散相，增加再结晶形核质点，使得 Wire-5E61 接头焊缝区晶粒细小，再结晶程度最高.

图 7 为 5E61 基材及 3 种焊丝接头焊缝区 XRD 图谱. 从图 7 可以看出，基材中除存在 α-Al 基体和 β 相 (Mg_2Al_3) 外，还含有少量 Mg_2Si，Al_6Mn 和 Al-(Fe,Mn)-Si 相，衍射峰明显；在 Wire-1561 接头焊缝区仅检测到 Al-(Fe,Mn)-Si 相和 Al_6Mn 相的衍射峰，且强度较弱；由于 Wire-5B71 焊丝成分中几乎不含

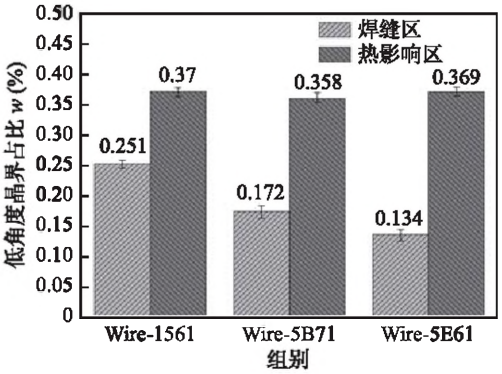

图 6 不同焊丝接头焊缝及热影响区的低角度晶界占比

Fig. 6 Proportion of low angle grain boundaries in WZ and HAZ of welded joints with different welding wires

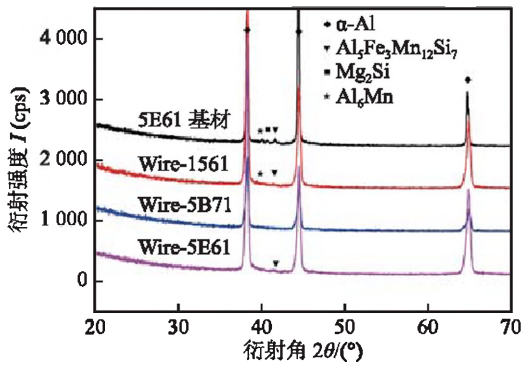

图 7 5E61 基材及不同焊丝接头焊缝区的 XRD 图谱

Fig. 7 XRD patterns of 5E61 base material and WZ of welded joints with different welding wires

Si 和 Mn 元素，在该焊缝区未检测到上述 3 种物相衍射峰；而在 Wire-5E61 接头焊缝区只检测到 Al-(Fe,Mn)-Si 的衍射峰. 另外，由于 Sc, Er 元素形成的析出相含量较少，X 射线衍射无法检测标定.

图 8 为 5E61 基材及 3 种焊丝接头焊缝区 SEM 形貌，并对图中 P1 ~ P9 点进行 EDS 成分分析，结果如表 3 所示. 5E61 基材第二相尺寸均匀，主要为 β 相 (Mg_2Al_3) 和 Al-(Fe,Mn)-Si 相，尺寸在 2 μm 以下. 从表 3 可知，Wire-5E61 接头焊缝区 α-Al 基体

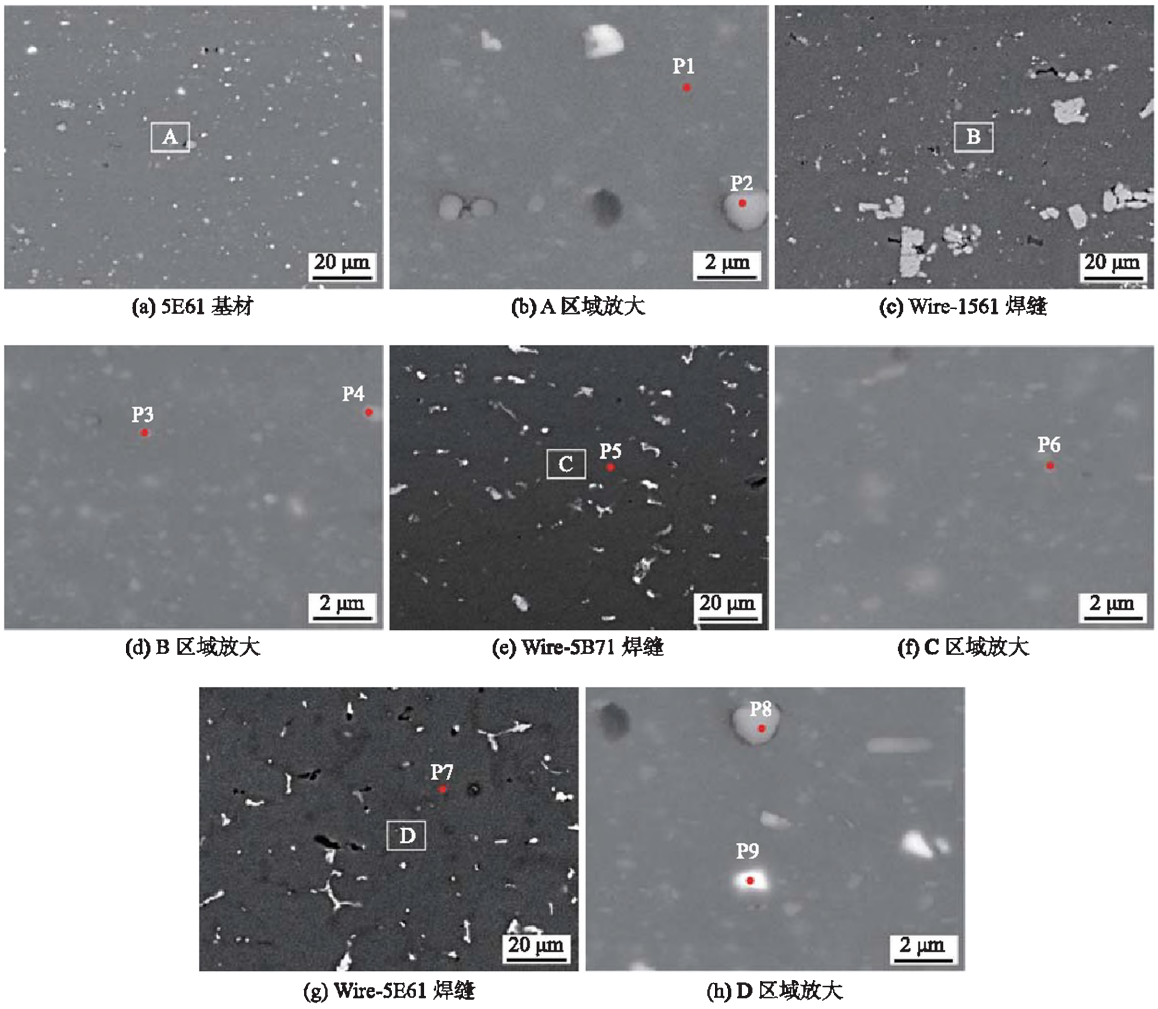

图 8 不同焊丝接头焊缝区 SEM 形貌

Fig. 8 SEM morphology of WZ microstructure with different welding wires. (a) 5E61 base material; (b) image of the selected area A; (c) WZ of Wire-1561; (d) image of the selected area B; (e) WZ of Wire-5B71; (f) image of the selected area C; (g) WZ of Wire-5E61; (h) image of the selected area D

表 3　EDS 测试结果 (质量分数，%)

Table 3　Results of EDS tests

位置	Al	Mg	Si	Fe	Mn	Er	Sc	Zr	可能物相
P1	92.13	5.25	0.42	0.38	1.82	—	—	—	α-铝基体
P2	77.48	2.84	3.51	7.40	8.77	—	—	—	β相、Al-(Fe,Mn)-Si
P3	87.78	5.32	—	—	6.90	—	—	—	β相、Al_6Mn
P4	83.27	5.07	—	3.64	8.02	—	—	—	β相、Al_6(Mn,Fe)
P5	93.97	6.03	—	—	—	—	—	—	α-铝基体
P6	78.33	4.83	—	5.62	3.34	—	4.76	3.12	β相、Al_3(Sc,Zr)
P7	93.82	6.18	—	—	—	—	—	—	α-铝基体
P8	79.48	4.02	—	10.72	5.78	—	—	—	β相、Al_6(Mn,Fe)
P9	67.43	4.40	—	—	9.52	13.28	—	5.37	β相、Al_3(Er,Zr)

中 Mg 含量最高，Wire-5B71 次之，Wire-1561 Mg 含量最低 (表 3 中 P2, P5, P7 点)，可见 TIG 焊接工艺下焊缝区主要由焊丝成分决定，随着焊丝中 Mg 含量的提高，焊缝区 α-Al 基体中固溶的 Mg 含量随之提高. 从图 8 可以看出，α-Al 基体中主要存在亮白色的 β 相 (Mg_2Al_3)，呈片状沿晶界析出，尺寸约为 4～6 μm. 通过对比可以看出，Wire-5E61 接头第二相比例最高，Wire-5B71 接头次之，Wire-1561 接头最低，其中 Wire-1561 焊丝接头焊缝区出现了一定程度的第二相聚集长大，这对焊缝区组织均匀性与焊缝力学性能不利. 图 8d、图 8f 和图 8h 分别为 3 种焊丝接头焊缝区高倍 SEM 形貌，可以发现焊缝组织中存在着大量白色析出相. EDS 测试结果显示，对于 Wire-1561 接头，析出相主要为 Al_6Mn；而对于 Wire-5B71和 Wire-5E61 接头，析出相分别为初生 Al_3(Sc,Zr)和 Al_3(Er,Zr)[10-11].

结合 3 种焊丝的合金成分，Wire-1561 焊丝中 Mn 元素含量接近 1%(0.94%)，在非平衡凝固下从基体中析出 Al_6Mn；对于 Wire-5B71 和 Wire-5E61 两种焊丝，由于 Sc 和 Er 元素的添加，在焊丝凝固过程中均发生共晶反应，形成 Al_3(Sc,Zr) 和 Al_3(Er,Zr) 纳米粒子，实现充分的溶质原子析出，为后续焊缝凝固组织提供大量异质形核点，有效细化焊缝枝晶组织，抑制晶粒长大，达到焊缝区细晶强化的目的.

2.3　焊接接头力学性能

图 9 为 3 种焊丝成分下的焊接接头显微硬度分布. 3 组接头的硬度分布变化趋势基本一致，均以焊缝中心为对称轴，呈对称分布. 5E61 基材显微硬度约为 98 HV；在焊缝区，Wire-5E61 焊丝接头平均显微硬度明显高于其余两组，约为 91 HV. 这是由于 Wire-5E61 中 Mg 元素含量最高，在相同的 TIG 焊接工艺下，Mg 元素的固溶程度最高，且焊丝中含有 Er 元素，形成大量均匀分布的 Al_3Er 纳米析出相，提供大量异质形核质点，实现焊缝凝固组织的晶粒细化，在固溶强化和细晶强化的双重作用下，焊缝硬度最大. 3 组接头均在熔合线位置达到硬度最小值，约为 84～86 HV. 由于在相同的焊接工艺下焊接热输入一致，致使 3 组接头热影响区宽度基本一致，且热影响区硬度值接近.

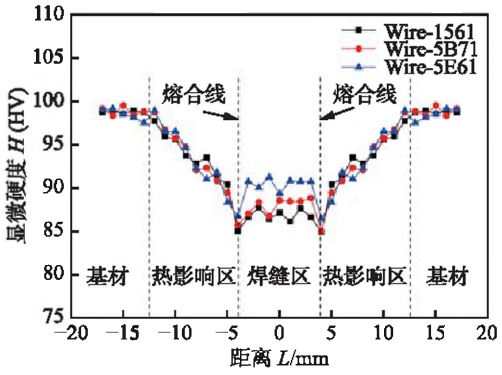

图 9　焊接接头的显微硬度

Fig. 9　Microhardness of welded joints

5E61 基材及不同成分焊丝下焊接接头的拉伸性能如表 4 所示. 5E61 基材的抗拉强度、屈服强度和断后伸长率分别为 386, 218 MPa 和 18.0%. Wire-1561, Wire-5B71 和 Wire-5E61 3 种焊丝接头的抗拉强度分别为 322, 323 和 338 MPa，屈服强度分别为 175, 173 和 177 MPa，断后伸长率分别为 13.0%, 14.5% 和 14.5%，焊接系数分别为 0.83,

表 4 5E61 铝合金基材和焊接接头的力学性能

Table 4 Mechanical properties of 5E61 aluminum alloy base material and welded joints

材料	屈服强度R_{eL}/MPa	抗拉强度R_m/MPa	断后伸长率A(%)	焊接系数φ
5E61基材	218	386	18.0	—
Wire-1561接头	175	322	13.0	0.83
Wire-5B71接头	173	323	14.5	0.84
Wire-5E61接头	177	338	14.5	0.88

0.84 和 0.88. 以上结果表明, Wire-5E61 焊接接头力学性能最优, 与焊缝处显微硬度一致.

图 10 为 3 组焊接接头拉伸试样的断裂位置. 从图 10 可以发现, Wire-5E61 接头均断在熔合线附近、距焊缝中心 3 ~ 5 mm 处, 且断口与熔合线平行; Wire-1561 接头和 Wire-5B71 接头个别试样断裂在焊缝处, 断口呈不规则形状. 在合适的焊接工艺条件下, 焊缝中心无明显缺陷, 拉伸断裂大部分发生在力学性能薄弱的熔合线位置.

图 11 为 3 组焊丝接头拉伸断口的微观形貌. 从图 11 可以看出, 在不同尺度层面下 3 种焊接接头的拉伸断口微观形貌均由大量的撕裂韧窝和少量的沿晶断裂构成, 未见较大解离面或者准解离特征形貌, 接头表现出良好的塑性, 均属于韧性断裂,

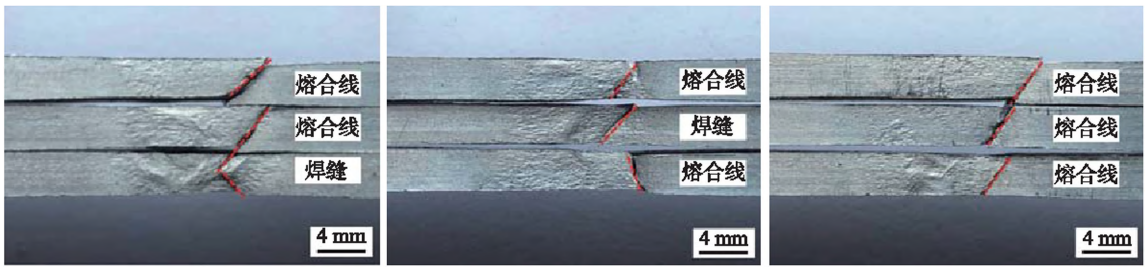

(a) Wire-1561 (b) Wire-5B71 (c) Wire-5E61

图 10 断裂位置

Fig. 10 Fracture location. (a) Wire-1561; (b) Wire-5B71; (c) Wire-5E61

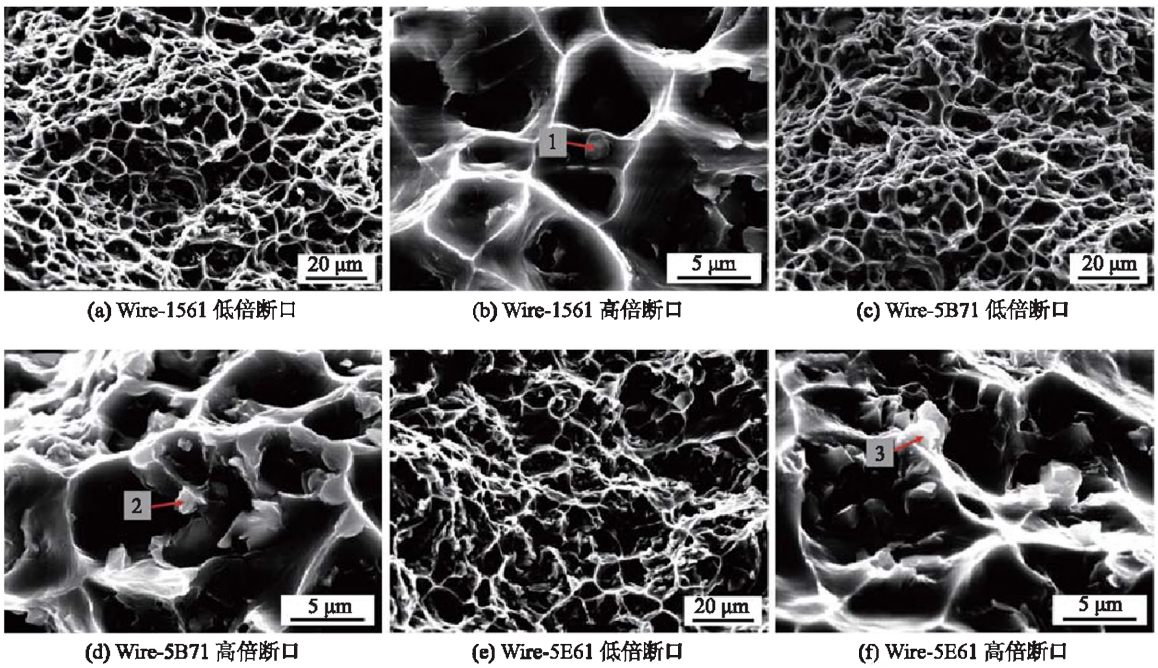

(a) Wire-1561 低倍断口 (b) Wire-1561 高倍断口 (c) Wire-5B71 低倍断口

(d) Wire-5B71 高倍断口 (e) Wire-5E61 低倍断口 (f) Wire-5E61 高倍断口

图 11 不同焊丝接头的断口微观组织

Fig. 11 Microstructures of joint fracture with different welding wires.(a) low magnification fracture of Wire-1561; (b) high magnification fracture of Wire-1561; (c) low magnification fracture of Wire-5B71; (d) high magnification fracture of Wire-5B71; (e) low magnification fracture of Wire-5E61; (f) high magnification fracture of Wire-5E61

断后伸长率均在 10% 以上. 由断口高倍放大图可以看出，韧窝处夹杂块状第二相粒子，如图 11 中 1，2，3 位置，EDS 测试结果如表 5 所示，表明第二相粒子多为含 Fe 高熔点粒子及铝镁氧化物等.

表 5　EDS 测试结果 (质量分数，%)

Table 5　Results of EDS tests

点	Al	Mg	O	Fe	Mn	可能物相
1	43.65	24.32	11.7	8.7	11.63	氧化物、$Al_6(Mn,Fe)$
2	40.12	19.35	23.21	9.43	7.89	氧化物、$Al_6(Mn,Fe)$
3	36.65	30.34	18.13	6.32	8.56	氧化物、$Al_6(Mn,Fe)$

3　结论

(1) 在相同的 TIG 焊工艺下，Wire-1561，Wire-5B71 和 Wire-5E61 3 种焊丝接头焊缝成形质量良好，焊缝中心无肉眼可见气孔，焊缝几何尺寸接近.

(2) 采用 Wire-5E61 和 Wire-5B71 制备的 TIG 焊接头由于 Er 和 Sc 元素形成的大量纳米颗粒，非均匀形核作用显著，接头焊缝区晶粒实现了不同程度地细化.

(3) 通过 TIG 焊方法，Wire-1561，Wire-5B71 和 Wire-5E61 3 焊丝接头的焊接系数分别为 0.83，0.84 和 0.88，断后伸长率分别为 13.0%，14.5% 和 14.5%，拉伸试样为韧性断裂，断口处存在大量韧窝，断裂位置主要沿熔合线附近的柱状晶区.

参考文献

[1] Xu P, Jiang F, Meng S, *et al*. Microstructure and mechanical properties of Al-Mg-Sc-Zr alloy variable polarity plasma arc welding joint[J]. Journal of Materials Engineering and Performance, 2018, 27(9): 4783 − 4790.

[2] 董春林, 赵运强, 温林秀, 等. 1561 铝合金搅拌摩擦焊接头微观组织分析 [J]. 焊接学报, 2020, 41(10): 1 − 5.
Dong Chunlin, Zhao Yunqiang, Wen Linxiu, *et al*. Study on microstructures of friction stir welded joint of 1561 aluminum alloy[J]. Transactions of the China Welding Institution, 2020, 41(10): 1 − 5.

[3] 雷玉成, 崔展祥, 路广遥, 等. 超声电弧对 6061 铝合金 MIG 焊接头组织和性能的影响 [J]. 焊接学报, 2020, 41(2): 33 − 38.
Lei Yucheng, Cui Zhanxiang, Lu Guangyao, *et al*. Effect of arc-ultrasonic on the microstructure and properties of 6061 aluminum alloy joint with MIG welding[J]. Transactions of the China Welding Institution, 2020, 41(2): 33 − 38.

[4] Liu Y, Wang W, Xie J, *et al*. Microstructure and mechanical properties of aluminum 5083 weldments by gas tungsten arc and gas metal arc welding[J]. Materials Science & Engineering A, 2012, 549(15): 7 − 13.

[5] Gungor B, Kaluc E, Taban E, *et al*. Mechanical and microstructural properties of robotic cold metal transfer (CMT) welded 5083-H111 and 6082-T651 aluminum alloys[J]. Materials and Design, 2014, 54: 207 − 211.

[6] 徐锴, 武鹏博, 梁晓梅, 等. 铝合金激光-多股绞合焊丝 MIG 复合焊特性分析 [J]. 焊接学报, 2021, 42(1): 16 − 23.
Xu Kai, Wu Pengbo, Liang Xiaomei, *et al*. Analysis of characteristics of aluminum alloy laser multi stranded welding wire MIG hybrid welding[J]. Transactions of the China Welding Institution, 2021, 42(1): 16 − 23.

[7] 王虎, 靳立坤, 彭云. 新型 Al-Mg-Mn-Er 合金 TIG 焊接头的微观组织及力学性能 [J]. 焊接学报, 2020, 41(3): 74 − 79.
Wang Hu, Jin Likun, Peng Yun. Microstructure and mechanical properties of joints of a new Al-Mg-Mn-Er alloy by TIG welding[J]. Transactions of the China Welding Institution, 2020, 41(3): 74 − 79.

[8] 闫德俊, 韩端锋, 王毅, 等. 1561 铝合金双面双弧 TIG 焊接接头的组织和力学性能 [J]. 中国有色金属学报, 2016, 26(10): 2065 − 2070.
Yan Dejun, Han Duanfeng, Wang Yi, *et al*. Microstructure and mechanical properties of 1561 aluminum alloy joints made by double-sided arc welding[J]. The Chinese Journal of Nonferrous Metals, 2016, 26(10): 2065 − 2070.

[9] 闫朝阳, 蒋凡, 陈树君, 等. 5E61 铝合金 VPPAW 焊接接头性能分析 [J]. 焊接学报, 2018, 39(2): 19 − 23.
Yan Zhaoyang, Jiang Fan, Chen Shujun, *et al*. Microstructure and mechanical properties of 5E61 aluminum alloy joint by VPPAW[J]. Transactions of the China Welding Institution, 2018, 39(2): 19 − 23.

[10] Wen S P, Wang W, Zhao W H, *et al*. Precipitation hardening and recrystallization behavior of Al-Mg-Er-Zr alloys[J]. Journal of Alloys and Compounds, 2016, 687: 143 − 151.

[11] 吴浩, 郑志凯, 任思蒙, 等. 微量 Er 和 Zr 对 Al-Mg 合金再结晶行为和焊接性能的影响 [J]. 中国有色金属学报, 2021, 31(2): 289 − 297.
Wu Hao, Zheng Zhikai, Ren Simeng, *et al*. Effects of Er and Zr micro-additions on recrystallization behavior and welding properties of Al-Mg alloy[J]. The Chinese Journal of Nonferrous Metals, 2021, 31(2): 289 − 297.

第一作者：毛晓东，硕士研究生；主要从事铝合金材料及焊接技术研究工作；Email:18600180450@163.com.

通信作者：谷宁杰，硕士研究生；Email: Guningjie@cmari.com.

（编辑：　戴红）

ing processes are complementary through the unique welding torch structure design. An external magnetic field was designed by regulating the coupling degree between two arcs for the problem of arc repulsion caused by different polarity of power supply in hybrid welding process to solve. The influence of main process parameters on the weld forming and section geometry characteristics of Q355B steel was studied. The results show that the external magnetic field can effectively improve the stability of the hybrid welding process and weld forming. FCAW voltage greatly influences the stability of the underwater hybrid welding process. Plasma welding current and FCAW voltage greatly influence weld penetration, and the plasma current has an approximately linear relationship with weld penetration. Compared with the underwater FCAW process, the welding depth of the hybrid welding process is increased by more than 40%, with higher welding efficiency and welding stability.

Highlights: (1) Plasma-FCAW hybrid welding technology suitable for underwater environment is proposed and a hybrid welding torch is designed.

(2) An external regulating magnetic field is analyzed to improve the repulsion between arcs and the arc strained condition.

(3) The influence of main process parameters on weld forming and section geometry characteristics is studied, and the welding efficiency of hybrid welding process is compared and analyzed.

Key words: plasma-FCAW; underwater hybrid welding; paraxial composite; magnetic field control; weld formation

Interfacial bonding properties of titanium foil/steel explosive welding BI Zhixiong[1], LI Xuejiao[1,2], WU Yong[1], XIONG Su[3], WANG Quan[1], RONG Kai[1](1. Anhui University of Science and Technology, Huainan, 232001, China; 2. Anhui Leiming Kehua Co., Ltd., Huaibei, 235000, China; 3. Guangzhou Engineering Design Institute, Guangzhou, 510000, China). pp 81-85

Abstract: To reduce titanium/steel explosive welding usage, the explosive welding between 200 μm thick TA1 titanium foil and Q235 steel was realized by using salt as a pressure transfer layer and low detonation velocity as a welding explosive. The microstructures at the interface were analyzed by metallographic microscope, scanning electron microscope and energy dispersive spectroscopy. Tensile and bending tests were carried out by a universal testing machine to test the bonding properties of the clad plate. The results show that the titanium foil/steel interface shows a regular waveform and is mainly bonded by the melting layer, which has good bonding quality. The metal near the interface produces strong plastic deformation, and the steel grains are linear. The vortex of the wave peak contains a melting block, and no holes or cracks are observed. According to the atomic ratio of Ti and Fe elements, the main components of melting block are FeTi and Fe_2Ti intermetallic compounds. The bonding interface did not separate when the three-point bending and tensile specimens were destroyed, which indicates that the clad plate has good plastic deformation ability and bonding performance. There are dimples of different sizes in the titanium and steel layers of tensile failure specimens, mainly plastic fractures.

Highlights: The explosive welding of 200 μm TA1 titanium foil/Q235 steel was carried out with salt as a pressure transfer layer, and the microstructure of the clad plate was analyzed.

Key words: explosive welding; pressure transfer layer; titanium foil; microtopography; bonding performance

Effect of welding wire composition on microstructure and properties of 5E61 aluminum alloy TIG welded joints MAO Xiaodong[1], GU Ningjie[1], SONG Xiaoyu[1], REN Simeng[1], LU Liying[2], LI Hutian[1](1. Chinalco Material Application Research Institute Co., Ltd., Beijing, 102209, China; 2. Northeast Light Alloy Co., Ltd., Harbin, 150060, China). pp 86-93

Abstract: To study the effect of welding wire composition on the microstructure and properties of 5E61 aluminum alloy ship plates welding joints, the tungsten intert-gas (TIG) welding of 4 mm 5E61-H116 aluminum alloy ship plate was conducted using Wire-1561, Wire-5B71 and Wire-5E61 welding wires. The welded joints' surface morphology, forming quality, microstructure, and mechanical properties were analyzed. The results showed that the welding quality of the three kinds of welding joints performed well under the same welding process,

and there were no visible porosities in the welding center zone. The microstructure of the welding zones was different. The grain size of the welding zone by Wire-5B71 was the smallest, followed by Wire-5E61, and the one of Wire-1561 was the largest. Due to the solution strength of the Mg element and the refined crystalline strength of Er element, the microhardness of the welding joint by Wire-5E61 performed the highest. The extension tests of welding joints have proceeded. The results showed the fracture locations of the joints were mainly located along the columnar crystal region near the fusion lines, where the microhardness displayed the lowest. The tensile strength of weld joints prepared by Wire-1561, Wire-5B71 and Wire-5E61 were 322, 323 and 338 MPa, respectively. The welding coefficients were 0.83, 0.84 and 0.88, respectively, and the elongations after fracture were 13.0%, 14.5% and 14.5%, respectively, which can meet practical engineering applications.

Highlights: (1) The weld strength of marine aluminum alloys with high magnesium can be improved by matching the composition of welding wires.

(2) Effect of element Mg, Er, Sc in the welding wires on the microstructure of 5E61 aluminum alloy joints welded by TIG welding was revealed.

Key words: 5E61 aluminum alloy; TIG welding; microstructure; mechanical properties

Mechanism of wire and arc interaction in hollow tungsten arc welding with coaxial filler wire YANG Yicheng[1,2,3], DU Bing[1], HUANG Jihua[2], HUANG Ruisheng[3], CHEN Jian[3], XU Fujia[3](1. China Academy of Machinery Science and Technology Group Co., Ltd., Beijing, 100044, China; 2. Lab. of Materials Welding and Joining, University of Science and Technology Beijing, Beijing, 100083, China; 3. Harbin Welding Institute Limited Company, Harbin, 150028, China). pp 94-99

Abstract: The interaction between welding wire and arc (wire-arc) is the key factor to determine the welding quality of hollow tungsten arc welding. Firstly, the shape of hollow tungsten electrode arc and solid tungsten electrode arc, and their influence on the weld forming characteristics are observed and analyzed by high-speed camera. Then the stress model of fuse process is constructed, the dynamic characteristics of droplet formation and transition process in coaxial wire filling welding are systematically analyzed. The research results show that the surface irradiation area of hollow tungsten electrode is larger than that of solid tungsten electrode, and the weld formation is stable under the high welding current. At the stage of droplet formation, the droplet at the end of the welding wire is in static equilibrium, and it cannot spontaneously transition from the end of the welding wire to the molten pool under the action of large surface tension. In droplet transition stage, part of the welding current flows through the welding wire, producing electromagnetic shrinkage force, causing the droplet swing between the welding wire and the molten pool.

Highlights: (1) The verification of hollow tungsten electrode welding with coaxial filler wire technology was completed for the first time.

(2) The evolution mechanism of welding wire and arc in the process of hollow tungsten electrode welding with coaxial filler wire is revealed by using high-speed camera.

Key words: hollow cathode; coaxial filler wire; droplet transfer; wire arc interaction

Three-dimensional measurement of post-weld surface based on grating projection YANG Guowei, ZHANG Jinli(Tianjin University of Science and Technology, Tianjin, 300222, China). pp 100-105,112

Abstract: The three-dimensional contour of the weld surface is an important index to evaluate the quality of the weld. In response to the problem that the measurement speed and accuracy cannot be balanced when the weld is measured by the commonly used line structured light scanning, a weld three-dimensional profile measurement system based on the surface structured light grating projection is designed and built. Firstly, the grating fringe is projected onto the weld through a digital light processing(DLP) projector, and the camera acquires the deformation modulation fringe. The phase of the deformed grating fringe is accurately calculated and unwrapped by using the four-step phase-shifting method combined with the multi-frequency heterodyne time-domain phase-resolving algorithm. Then, using a planar target combined with a high precision